Article

Deformation Behavior and Microstructure Evolution of CoCrNi Medium-Entropy Alloy Shaped Charge Liners

Jian Chen [1,2], **Tian-Wei Liu** [1,2], **Fu-Hua Cao** [1,2], **Hai-Ying Wang** [1,2], **Yan Chen** [1,2] **and Lan-Hong Dai** [1,2,*]

1   State Key Laboratory of Nonlinear Mechanics, Institute of Mechanics, Chinese Academy of Sciences, Beijing 100190, China; chenjian@imech.ac.cn (J.C.); liutianwei@lnm.imech.ac.cn (T.-W.L.); caofuhua@imech.ac.cn (F.-H.C.); why@lnm.imech.ac.cn (H.-Y.W.); chenyan@lnm.imech.ac.cn (Y.C.)
2   School of Engineering Science, University of Chinese Academy of Sciences, Beijing 101408, China
*   Correspondence: lhdai@lnm.imech.ac.cn

Abstract: To investigate the microstructure evolution and dynamic deformation behavior of a CoCrNi medium entropy alloy under an ultrahigh explosive loading rate, CoCrNi-shaped charged liners were fabricated and fired into steel targets. Targets with residual jet fragments were recovered for detailed microstructural analysis using scanning electrical microscopy, X-ray diffraction, electron backscattered diffraction, and transmission electron microscopy. The results indicate that the grain size was reduced by more than 3 times and grains were found to be equiaxed in the residual jet, which indicates that dynamic recrystallization (DRX) occurred during this extremely high strain rate and large plastic deformation. Furthermore, the content of Cr element in CoCrNi at the grain boundaries increased significantly after detonation deformation. The reduced grain sizes are believed to reduce the bulk diffusion path of Cr from grain interior into grain boundaries with the support of sufficient energy provided by the ultrahigh temperature. The enrichment of Cr at grain boundaries promotes the formation of nanosized Cr-rich precipitates with body-centered cubic (BCC) structures, which were found to be widely distributed along grain boundaries in the residual jet. These precipitates were considered obstacles for grain boundary movement and promotion of crack initiation along the grain boundaries, which might cause ductility loss of the CoCrNi-shaped charge jet and loss of penetration capability.

Keywords: shaped charge liner; CoCrNi; ultrahigh strain rate; nanosized precipitation

1. Introduction

Shaped charge liners (SCLs) have been widely used in many fields such as the oil industry, mining, and construction engineering [1–3]. Different from general deformation cases, the deformation of an SCL in the shaped charge scheme is under an extreme condition, where the strain rate reaches up to 10^5 s^{-1}, and the strain exceeds 5 [4]. In the process of explosive detonation, the liberation of heat rapidly increases the temperature of an SCL, and the high-pressure (over 20 GPa) detonation wave collapses the liner materials to form a shaped charge jet. Thus, the shaped charge provides a desirable experimental scheme for investigating the deformation behavior of materials under extreme conditions, combining an ultrahigh strain rate, strain, pressure, and temperature.

The extreme plastic deformation experienced by an SCL in the shaped charge scheme is generally considered to be superplastic deformation at high strain rates [5,6]. Chokshi and Meyers et al. [7] demonstrated that the extraordinarily high strains experienced by the shaped charge can be explained by high strain rate superplasticity, which is induced by a drastic grain size reduction produced by dynamic recrystallization (DRX). DRX was believed to accommodate the solid-state flow that exists in severe plastic deformation, particularly involving high strain rates [8–10]. Murr et al. [11] observed equiaxed grains and grain size reduction in recovered jet fragments compared to the initial SCL, and

they suggested that DRX plays an important role in jet elongation and microstructure evolution. Apart from the grain size reduction and the appearance of equiaxed grains, grain boundary activities are also closely related to the DRX. Liaw et al. [12] demonstrated that grain boundary sliding and DRX are responsible for the large elongation in superplastic deformation. Above all, the microstructure evolution has a significant influence on the deformation behavior of the shaped charge jet in addition to the penetration capability.

The existing research suggests that shaped charge liner materials should have a good combination of high density, sound speed, and plasticity [13,14], and some new shaped charge liner materials have been developed [15,16]. High-entropy alloys (HEAs) are a new type of alloy composed of four or more elements in near equiatomic ratios with a high mixing entropy. The addition of more elements in conventional alloys usually produces brittle intermetallic compounds that deteriorate mechanical properties, such as the Heusler alloys [17–19]. The high mixing entropy in HEAs can increase the compatibility between the principal elements, which allows tailoring the distribution and property of intermetallic compounds [20]. The topologically ordered lattice structure and random arrangement of multi-element atoms bring many unique performances to HEAs [21–26], which makes it a promising candidate for shaped charge liners. Different from the topological disorder in amorphous alloys [27], the high-entropy alloys are controlled by chemical disorder. HEAs are usually prepared by smelting the high-purity metal mixture in a vacuum with arc heat. Over the past several years, mechanical and performance breakthroughs have been made during HEA exploration, illustrating their potential to replace traditional materials in many fields [28–33]. Previous research on HEAs focused on the deformation behavior and microstructure evolution primarily based on quasi-static and dynamic testing, where the strain rate was lower than 10^5 s^{-1}. Qiao et al. [34] revealed the dynamic behavior of CrMnFeCoNi HEA in impact tension using a split Hopkinson tensile bar with high-speed photography. Jiang et al. [35] studied the shock response and obtained the Hugoniot equation of state of two HEAs for the first time, which provides new insight into the shock compression behavior of HEAs. In addition to the Cantor HEA, HEAs with different compositions also exhibit unique structural and performance characteristics. Senkov and Liaw et al. [36] developed two refractory HEAs with near-equatomic concentrations, the microhardness of which is greater than that of any individual constituent. Zhang et al. [37] analyzed the penetration behaviors of WFeNiMo HEA which exhibits self-sharpening behavior. As a subset of common Co-Cr-Fe-Mn-Ni systems, the medium-entropy alloy (MEA) CoCrNi exhibited superior mechanical properties in some aspects [38–40]. Equiatomic MEA CoCrNi with an FCC single phase indicates a preferable combination of high ductility, density (7.6 g·cm^{-3}), and sound velocity, which makes it a promising candidate as shaped charge liner. Cao et al. [40] revealed the atomic-scale mechanisms of incipient plasticity in CoCrNi MEA. However, research on the ultrahigh strain rate deformation behavior and microstructure evolution of CoCrNi has not been conducted.

To investigate the dynamic behavior and microstructure evolution of ternary CoCrNi MEA under explosive loading conditions, CoCrNi liners were fabricated and fired into steel targets. The microstructural changes in the SCL after detonation were investigated by comparing the microstructures of the initial SCL and recovered residual jet. The microstructural changes in CoCrNi alloys under ultrahigh strain rate deformation were also analyzed in this research.

2. Materials and Methods

2.1. Preparation of the CoCrNi SCL

The equiatomic CoCrNi MEA was prepared from raw materials with a purity of 99.9% using a vacuum magnetic levitation melting device. The CoCrNi ingot was remelted in a high-purity argon atmosphere four times and homogenized at 1250 °C for 50 min to ensure good composition homogeneity. Afterward, the ingot was forged longitudinally into a rod with a diameter of 65 mm. After testing, the density of the sample was 7.6 g/cm^3 and it had good tensile strength and plasticity (σ_f = 900 MPa and ε_f = 42%). A conical CoCrNi shaped

charge liner with a width of 60 mm and cone angle of 60° was mechanically machined from the rod.

2.2. Explosive Detonation

Composition B explosive (consisting of mixtures of 60% RDX and 40% TNT) was used for the explosive detonation. The density, detonation pressure, and detonation velocity of Com B are 1.74 g·cm^{-3}, 25.9 GPa, and 7.9 km·s^{-1}, respectively. For penetration, a standard high-strength carbon structural steel (C45E4 steel) with tensile strength greater than 600 MPa was prepared as the target. Figure 1a schematically demonstrates the longitudinal section of the deformation process of the CoCrNi-shaped charge jet. Upon detonation, a spherical detonation wave with high pressure propagated and collapsed the conical CoCrNi SCL to flow in the form of a jet in excess of 7 km·s^{-1}. The CoCrNi-shaped charge jet formed along the axis of the cone and fired vertically into the steel target at a stand-off of 200 mm to form a crater. After penetration, the surface of the crater was covered by a CoCrNi residual jet, as displayed in Figure 1b. The steel targets were recovered and cut along the longitudinal axis of the crater by electrical discharge machining after penetration.
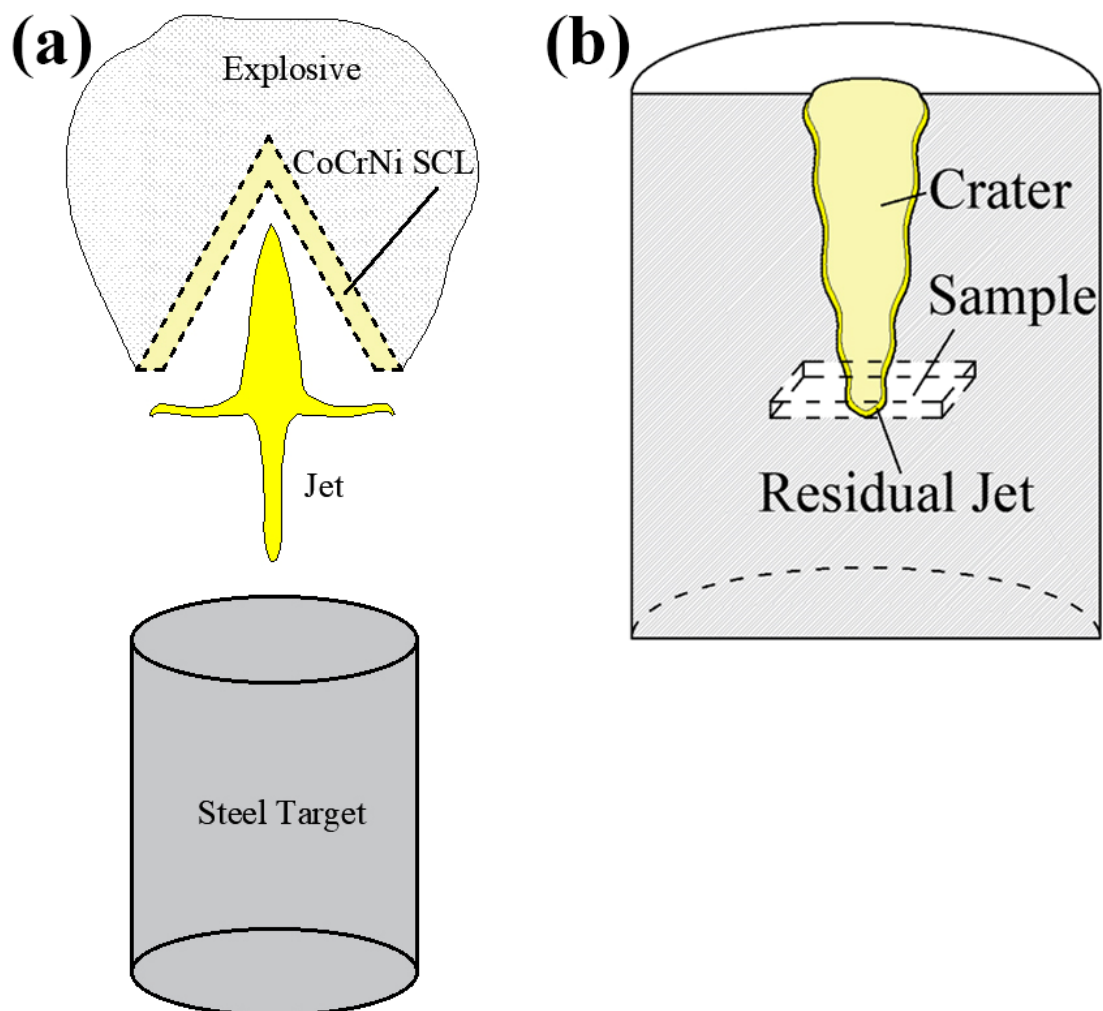

Figure 1. Schematic diagram of the CoCrNi shaped charge scheme (**a**) and the cross-section of half of the recovered steel target cut along the penetration direction. The sample for later microstructure characterization is marked by the dashed line in (**b**).

2.3. Microstructure Characterization

The microstructural changes in CoCrNi shaped charges during jet formation and penetration significantly reflect the extreme plastic deformation mechanism. Thus, we compared the microstructures of the CoCrNi shaped charge liner before and after detonation deformation, which were represented by the residual jet. The samples of the initial SCL and residual jet were cut perpendicular to the penetration direction from the ternary CoCrNi rod and the bottom of the crater by electrical discharge machining, respectively. Figure 1b illustrates the cutting scheme of the residual jet. X-ray diffraction (XRD, Rigaku Dmax 2500, Rigaku, Tokyo, Japan) using a Cu Kα target was used to identify the phase composition of the initial CoCrNi SCL and the residual jet. Scanning electron microscopy (SEM), electron backscattered diffraction (EBSD), and transmission electron microscopy (TEM) with an energy dispersive spectrometer (EDS) were used to reveal microstructures in the CoCrNi SCL and residual jet. The specimens used for TEM observation were obtained using a focused ion beam (FIB) instrument (FEI Helios Nanolab 600i, FEI, Oregon, America). EBSD observation was conducted using a field SEM equipped with an EDAX-TSL OIM EBSD system (EDAX, OIM Analysis 6.0).

3. Results

3.1. Initial Microstructures of CoCrNi SCL

The structural characteristics of the initial CoCrNi SCL were determined using EBSD, TEM, and XRD. As indicated in Figure 2a, the inverse pole figure (IPF) map indicates a random orientation distribution of grains in the initial SCL. Grains in the initial SCL are essentially columnar and equiaxed, and the average grain size is 16 μm. The elemental distributions of the initial SCL are illustrated by a representative high-angle annular dark-field (HAADF) image with EDS analysis in Figure 2c. The results indicate that Co, Cr, and Ni elements were distributed uniformly in the initial microstructures without element segregation, nanoclusters, or second phase. The XRD patterns of samples from the initial SCL and residual jet are presented in Figure 2d, which illustrates only regular FCC peaks.
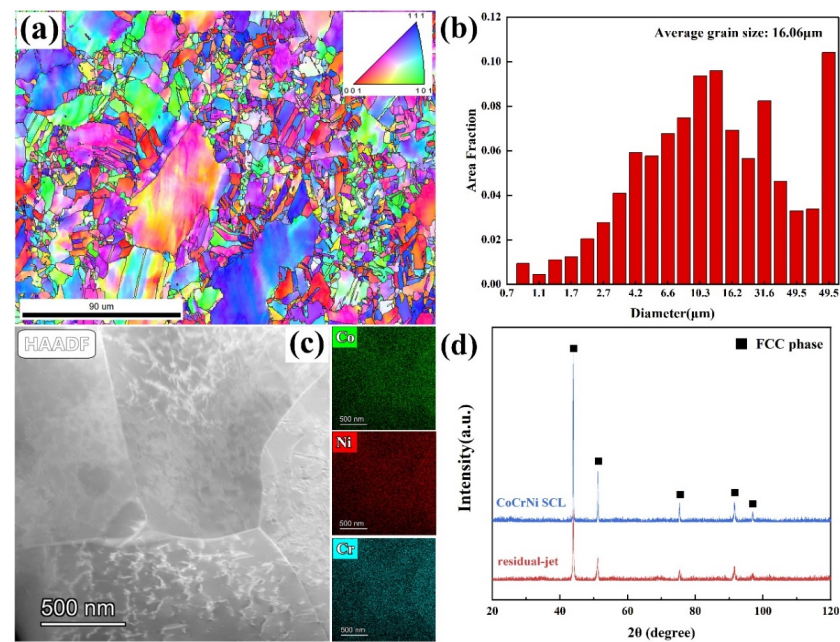

Figure 2. Microstructures and phase compositions of the initial CoCrNi liner. (**a**) EBSD image of the initial CoCrNi liner, indicating an average grain size of 16 μm. (**b**) Histogram of statistical grain size. (**c**) HAADF image and element distributions of Co, Cr and Ni. (**d**) XRD results of CoCrNi liners before and after penetration.

3.2. Microstructures in the Residual Jet

The macroscopic SEM image (Figure 3a) displays structural details in the bottom part of the jet crater, which is observed along the penetration direction. The surface of the crater is coarse due to severe interaction between the jet and target. A magnified image of the region, marked by the red frame in Figure 3a, is displayed in Figure 3b. The boundary between the steel target and residual jet can be observed clearly, and is marked by a white line. To further identify the boundary, the residual jet region is characterized by EDS map analysis (Figure 3c). The results indicate that a residual jet region with a width of approximately 30 μm sticks to the steel target crater. According to the XRD results (Figure 2d), no obvious phase transformation occurred during the detonation deformation.
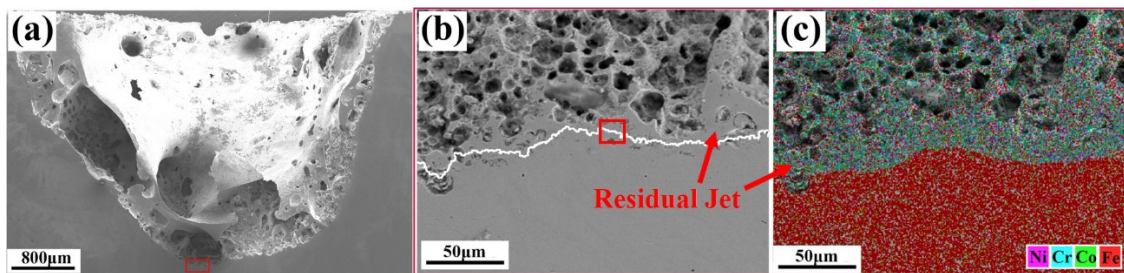

Figure 3. SEM image of the CoCrNi residual jet after penetration observed along the penetration direction at the bottom of the jet crater. The residual jet region is marked by the red arrow in (**b**) and (**c**). (**a**) SEM image of the bottom of the jet crater. (**b**) Magnified view of the region marked with a red rectangle in (**a**). (**c**) SEM-EDS mapping of (**b**).

Figure 4a displays the EBSD orientation map of the region marked with a red rectangle in Figure 3b. The solid white line in Figure 4a is presented as the boundary between the residual jet and steel target, which is marked as region a3. According to the microstructural characteristics, the residual jet can be divided into two zones: the recrystallization zone and deformation zone, which are separated by the white dashed line and labeled a1 and a2 in Figure 4a, respectively. It is worth mentioning that the deformation here refers to the deformation of the jet caused by the interaction between the jet and the target during the penetration process. The deformation zone was created by the transverse interaction of the CoCrNi-shaped charge jet with the sidewall of the steel target. Thus, the width of the deformation zone reflects the intensity of the transverse interaction between the jet and target and the transverse dissipation of the jet energy [16,41]. Figure $4b_1,c_1$ present magnified images of marked regions a and b in Figure 4a, respectively. After penetration, the residual jet was characterized by two kinds of grains, which are equiaxed recrystallized grains in the recrystallization zone (a1) and small deformed grains in the deformation zone (a2), which exhibit significant twisting and stretching. According to the EBSD data, the average grain size of the recrystallized grains is approximately 4.4 μm, and the grain size of the small grains ranges from 200 nm to 2 μm. It is clearly demonstrated that the CoCrNi SCL experienced a severe grain size reduction from 16 μm to less than 5 μm during penetration. Kernel average misorientation (KAM) maps are good indicators of the distribution of defects and local misorientations in alloys. The corresponding KAM maps of regions b and c in Figure 4a are displayed in Figure $4b_2,c_2$, respectively, and both KAM maps were drawn with the first nearest neighbor. The color in the KAM maps ranges from blue to red, corresponding to KAM values from 0° to 5°. The KAM map of region b is indexed by deep blue, indicating a small KAM value close to 0 in the recrystallized grains. Similarly, the KAM map of the residual jet in region c is also dominated by the blue color, and only a small part near the boundary with the steel target is green. It can be concluded that the dislocations and defects in the residual jet are seldomly and uniformly distributed, which corresponds to the elimination of dislocations during the DRX process experienced by the shaped charge jet.
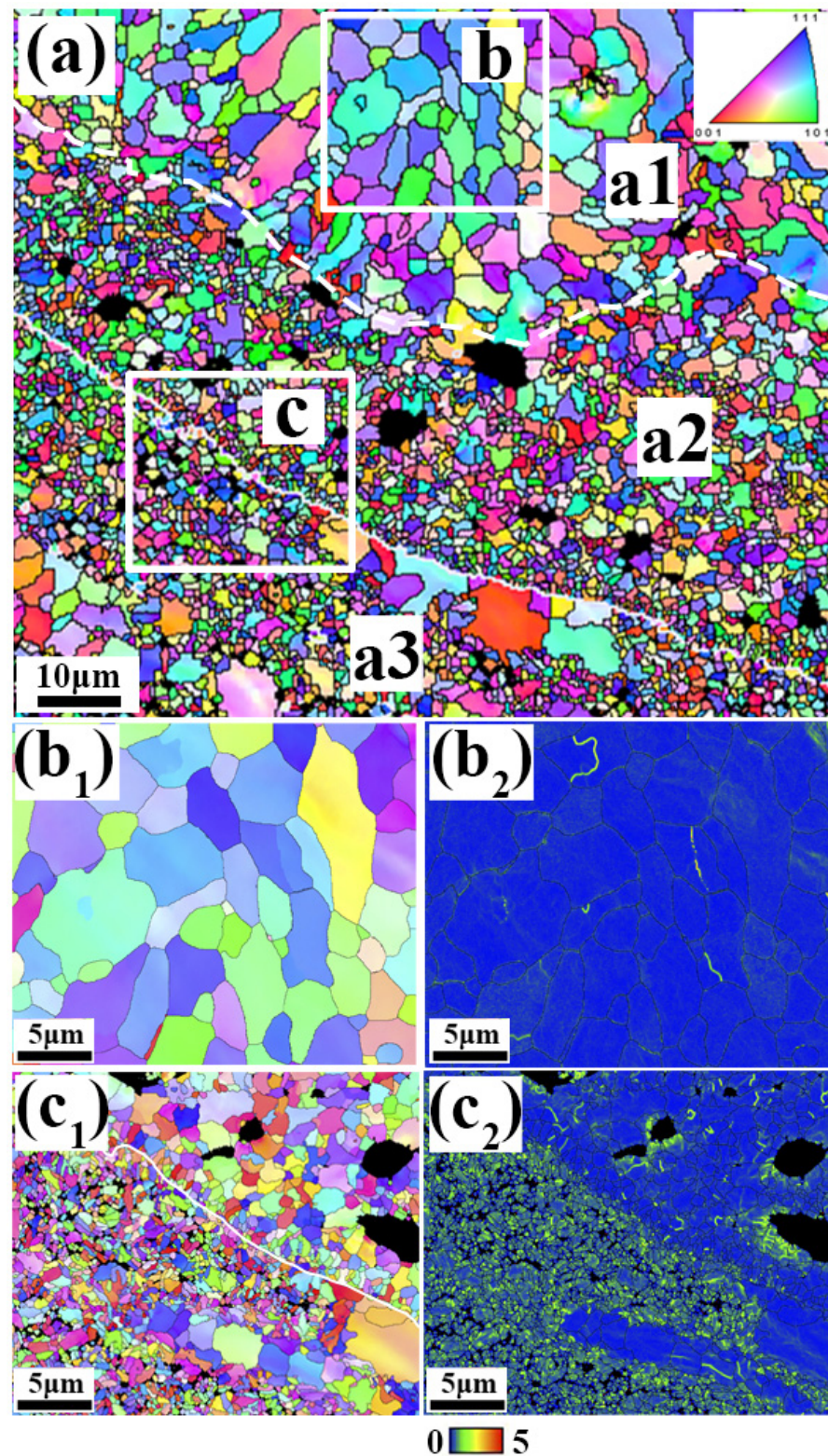
Figure 4. Microstructural analysis of the residual jet after penetration via EBSD: (**a**) IPF map of microstructures marked in rectangle in Figure 3b; (**b₁,b₂**) IPF map and corresponding KAM map of region b in (**a**); (**c₁,c₂**) IPF map and corresponding KAM map of region c in (**a**). The dashed line in (**a**) represents the boundary between regions a1 and a2, and the white solid line indicates the steel target (region a3) and residual jet (regions a1 and a2).

3.3. Grain Boundary Precipitations

To further investigate the microstructural changes in the CoCrNi SCL during detonation deformation, high-magnification backscattered electron (BSE) imaging of the recrystallized grains of the residual jet (region b in Figure 4a) was used and the results are displayed in Figure 5a. It can be observed that the grains are equiaxed and the grain size is smaller than 1 μm. Furthermore, an SEM-EDS line scan was performed on the same sample along the yellow line in Figure 5a. The scan path passed through a complete grain and two grain boundaries. The element distributions of Cr, Co, and Ni along the scan path are displayed in Figure 5b, where the dashed line was used to mark the location of the grain boundaries. Different from the uniform distribution of Cr, Co, and Ni in the initial CoCrNi SCL, the distribution of Cr at the grain boundaries increased significantly and the distribution of Co and Ni apparently decreased in the residual jet. It is reasonable to speculate that the inhomogeneous distribution of elements is closely related to the deformation mechanism of the CoCrNi-shaped charge jet.
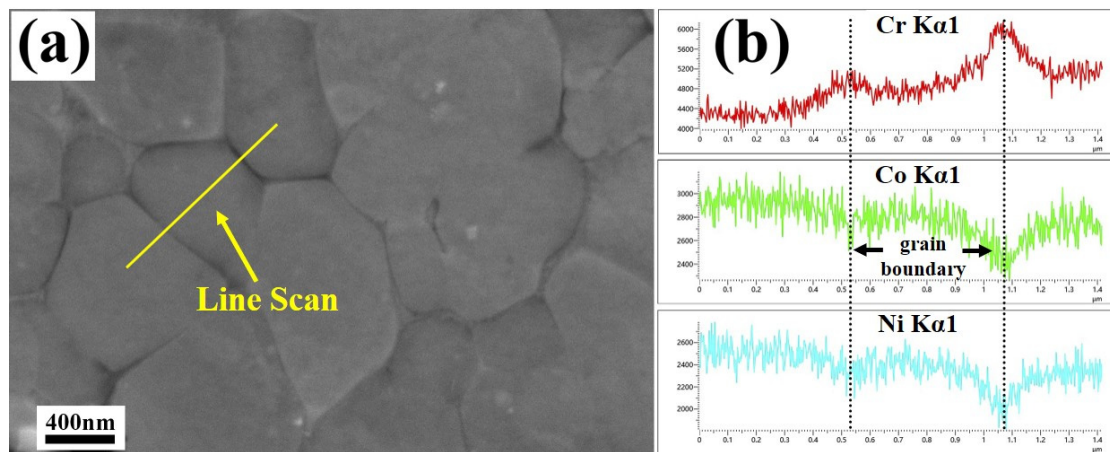

Figure 5. High-magnification BSE-SEM images (**a**) and line scan analysis (**b**) of the recrystallization region (Region b in Figure 4a). A line scan was conducted across two grain boundaries as displayed in (**a**), the corresponding locations of which are labeled with dashed lines in (**b**).

To determine the reason for the inhomogeneous element distribution in the residual jet, TEM analyses were performed on an FIB sample of the residual jet. Figure 6a displays a bright-field TEM image of microstructures in the residual jet. No obvious dislocation structures or twins were observed in the residual jet. Nanosized precipitations with different contrasts can be observed along the grain boundaries, and the precipitation is marked with white dashed lines in Figure 6a. It can be observed that the precipitation is widely distributed along grain boundaries with widths of 20~60 nm. For further determination of the constitution of the precipitation, we took EDS maps of the precipitation marked with the red square in Figure 6a. The magnified view of the precipitation marked in Figure 6a is displayed in Figure 6b, and the element distributions of Co, Ni, and Cr are presented in Figure 6c–e. The results indicate that the content of Cr in the precipitation is dramatically higher than that of Co and Ni, which is consistent with the prior SEM-EDS results displayed in Figure 5b. To specifically reveal the element constitution in the residual jet near the precipitation, we conducted EDS analysis on the matrix region (II, III, and IV) and precipitation region (I) in Figure 6b. The EDS results of these four regions are presented in Figure 6g, which indicates that the content of Cr in the precipitation region (I) reached 80%, while the average content of Cr in the matrix regions (II, III, and IV) was only 24%, which is lower than the original content of 33% in the initial SCL. The difference in the chemical distribution around the grain boundary indicates that atomic migration took place at the grain boundary, and Cr transferred from the grain interior to the grain boundary under the action of high temperature during penetration. The selected

area electron diffraction (SAED) pattern taken from region I in Figure 6b is displayed in Figure 6f. The SAED pattern exhibits a body-centered cubic (BCC) structure pattern, which indicates that the precipitate is a nanosized phase with a BCC structure.
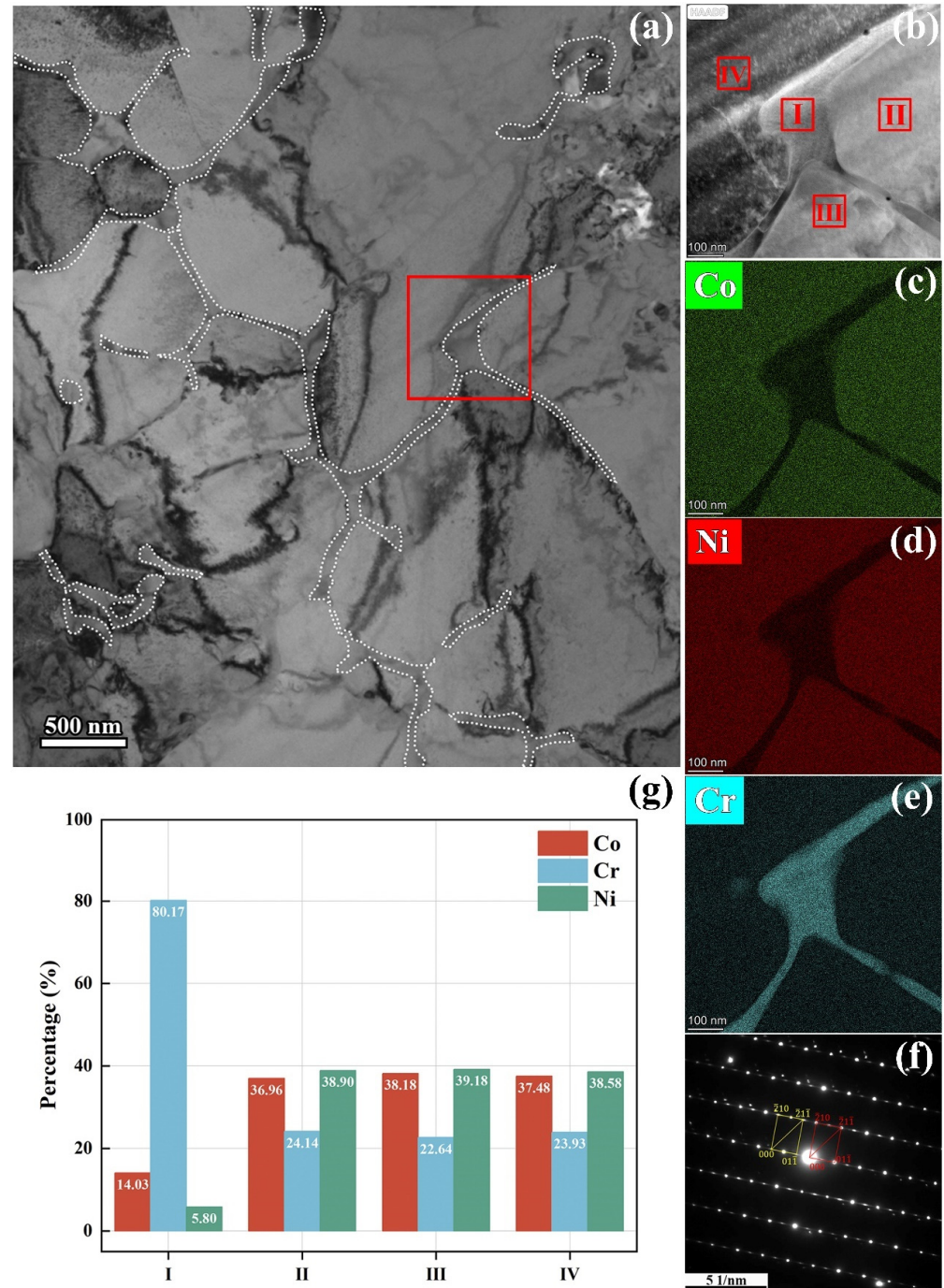

Figure 6. Microstructural analysis of CoCrNi residual jet after penetration by TEM: (**a**) TEM images of CoCrNi residual jet; (**b**) HAADF-TEM image of the precipitation (red rectangle region in (**a**)); (**c**–**e**) Corresponding element distributions of Co, Cr, and Ni in (**b**); (**f**) SAED pattern of precipitation (region I in (**b**)); (**g**) Element content of Co, Cr, and Ni in region I, II, III, IV in (**b**). The white dashed line in (**a**) marks the nanosized precipitations along grain boundaries.

4. Discussion

4.1. Dynamic Recrystallization in CoCrNi Shaped Charge Detonation

Dynamic recrystallization has been generally observed in severe plastic deformation, particularly at high strain rates ($>10^3$ s^{-1}) such as the shaped charge regime [42–44]. Grain size reduction induced by dynamic recrystallization in shaped charge liners is a common phenomenon during shaped charge detonation. Murr et al. [43] examined the starting liner-cone grain sizes and grain structures with recovered slugs and jet fragments from a detonated tantalum-shaped charge and reported a great grain size reduction in the tantalum-shaped charge by as much as a factor of 100. In this work, the grain size decreased from 16 μm in the initial SCL to less than 5 μm in the residual jet. The EBSD results (Figures 2 and 4) indicate a transformation from coarse columnar grains in the initial SCL to fine equiaxed grains in the residual jet. Considering the severe plastic deformation in the detonation deformation, we can postulate that dynamic recrystallization took place in the CoCrNi-shaped charge liner during shaped charge deformation. According to the microstructure characteristics, the CoCrNi residual jet can be divided into the following two regions: the recrystallization region (region a1 in Figure 4a) and the deformation region (region a2 in Figure 4a). The EBSD results (Figure 4b$_2$,c$_2$) indicate that the KAM values in the recrystallization region and deformation region are both close to 0, which indicates that there are few dislocations in the whole residual jet. Thus, it can be concluded that the DRX that occurred during shaped charge deformation consumed a large number of dislocations. Furthermore, the elongated grains of the residual jet at the boundaries with the steel target deform in the direction perpendicular to the boundaries. Therefore, the grain refinement and irregular deformation in the deformation region were caused by the interaction between the jet and steel target. In conclusion, dynamic recrystallization constitutes the most evident mechanism characterizing CoCrNi-shaped charge deformation.

4.2. Cr-Rich Grain Boundary Precipitation

At the beginning of detonation, a high-pressure explosive wave collapsed the initial SCL and forced it to act like a solid-state fluid [42]. The shaped charge jet experienced a high strain rate and severe plastic deformation under the condition of high temperature before penetration. The penetration ability of the shaped charge is largely related to the ductility of the shaped charge, which makes it essential to determine the deformation mechanism of the shaped charge jet. The large strain deformation experienced by the shaped charge jet is believed to be accommodated by grain boundary sliding [7,45]. During the severe plastic deformation in the shaped charge process, the refined grain structure caused by dynamic recrystallization can easily rotate and slide past each other to accommodate the large strains. From this perspective, the movement of grain boundaries has a great effect on the penetration ability of shaped charges. The impact of nanosized precipitates at grain boundaries on the movement of grain boundaries is of vital importance on the penetration behavior of CoCrNi-shaped charges.

Generally, the CoCrNi MEA possesses an excellent phase stability with a stable single FCC phase structure [46]. However, Li et al. [47] investigated the phase decomposition of a nanocrystalline CoCrNi alloy and found that phase decomposition occurs faster in smaller grains, which enables fast diffusion in addition to short circuit transport. In this research, grain size reduction is an unambiguous phenomenon in shaped charge penetration. The reduced grain sizes in the shaped charge jet reduced the bulk diffusion path of Cr, which enabled fast diffusion of Cr away from the grain interior to the grain boundaries under the condition of high temperature during shaped charge deformation [48,49]. Additionally, the ultrahigh temperature provided sufficient energy for the diffusion of Cr atoms into grain boundaries and reduced the time needed. The enrichment of Cr at grain boundaries promotes phase decomposition in the shaped charge jet and the formation of the Cr-rich bcc phase [50]. It is worth mentioning that the fast diffusion of Cr to the grain boundaries in the CoCrNi-shaped charge jet is also supported by the diffusivity of elements. According to Tsai et al.'s research [51], Cr possesses a higher diffusion coefficient than Co and Ni in

CoCrFeMnNi. In most cases, the precipitation of second phases at grain boundaries induces the incompatibility of elastic and plastic deformation between the matrix and particles, which causes high stress/strain concentrations and ductility reduction in metals and alloys [52]. Ming et al. [53] reported that Cr, Ni, and Mn nanoclusters at grain boundaries reduce grain boundary cohesion and promote crack initiation along grain boundaries, which leads to ductility loss in the CrMnFeCoNi HEA upon deformation at intermediate temperatures. As a consequence, the Cr-rich bcc precipitates in the grain boundaries of the CoCrNi-shaped charge jet are believed to act as an obstacle for grain boundary sliding and promote crack initiation along grain boundaries, which causes a loss of ductility of the CoCrNi-shaped charge jet in addition to the ability of penetration.

5. Conclusions

The microstructure evolution of the novel CoCrNi SCL under an ultrahigh strain rate and strain detonation deformation was studied here for the first time. The grain size reduction occured by a factor of more than 3 in the CoCrNi SCL during detonation deformation. Different from the existing research on the pure metal or traditional alloy SCL, the ternary CoCrNi MEA SCL is composed of three elements with equal atomic percentages. The multiprinciple element constitutions of CoCrNi lead to distinctive microstructure evolution in detonation deformation, which provides valuable references for understanding the mechanism in the shaped charge scheme. The main findings are concluded as follows:

1. The CoCrNi SCL experienced a severe grain size reduction from 16 μm to less than 5 μm during penetration. After penetration, the residual jet was composed of equiaxed grains in the recrystallization zone and elongated grains within the deformation zone. Dislocations were few and were distributed uniformly in residual jet.
2. An obvious dynamic recrystallization phenomenon was observed in residual jet, which led to a severe grain size reduction. The refined grain structures are supposed to accommodate the large strains in the severe plastic deformation of the shaped charge jet.
3. Compared to the initial SCL, the content of Cr at the grain boundaries in the residual jet increased significantly, while the content of Co and Ni decreased. Furthermore, the nanosized Cr-rich precipitates with BCC structures were observed to be widely distributed along grain boundaries. The reduced grain size reduced the bulk diffusion path of Cr from grain interior to the grain boundary. The Cr-rich precipitations were considered obstacles for grain boundary movement and promotion of crack initiation along the grain boundaries, which depleted the ductility of the CoCrNi-shaped charge jet and its ability to penetrate.

Author Contributions: Conceptualization, L.-H.D.; Investigation, J.C., L.-H.D., H.-Y.W. and Y.C.; methodology, J.C.; validation, J.C., T.-W.L., F.-H.C., H.-Y.W., Y.C. and L.-H.D.; data curation, J.C.; writing—original draft preparation, J.C.; writing—review and editing, L.-H.D., T.-W.L. and F.-H.C. All authors have read and agreed to the published version of the manuscript.

Data Availability Statement: Not applicated.

Conflicts of Interest: The authors declare no conflict of interest.

References

1. Jiao, W.; Chen, X. Review on Long-Rod Penetration at Hypervelocity. *Adv. Mech.* **2019**, *49*, 312–391. [CrossRef]
2. Meyers, M.A. *Dynamic Behavior of Materials*; Wiley: Hoboken, NJ, USA, 1994; ISBN 9780471582625.

3. Li, G.; Chen, X.W. Selection and Analysis of Material Models in Copper Jet Penetration into Water. *J. Phys. Conf. Ser.* **2020**, *1507*, 032017. [CrossRef]

4. Murr, L.E.; Niou, C.S.; Garcia, E.P.; Ferreyra, E.T.; Rivas, J.M.; Sanchez, J.C. Comparison of Jetting-Related Microstructures Associated with Hypervelocity Impact Crater Formation in Copper Targets and Copper Shaped Charges. *Mater. Sci. Eng. A* **1997**, *222*, 118–132. [CrossRef]

5. Song, P.; Li, W.B.; Zheng, Y.; Song, J.P.; Jiang, X.C.; Yan, B.Y. Study on Plastic Deformation Behavior of Mo-10ta under Ultra-High Strain Rate. *Metals* **2020**, *10*, 1153. [CrossRef]

6. Meyers, M.A.; Meyer, L.W.; Vecchio, K.S.; Andrade, U. High Strain, High Strain-Rate Deformation of Copper. *J. Phys. IV Proc.* **1991**, *1*, C3-11–C3-17. [CrossRef]

7. Chokshi, A.H.; Meyers, M.A. The Prospects for Superplasticity at High Strain Rates: Preliminary Considerations and an Example. *Scr. Metall. Mater.* **1990**, *24*, 605–610. [CrossRef]

8. Shih, H.K.; Murr, L.E.; Niou, C.S.; Zernow, L. Dynamic Recrystallization in a Tantalum Shaped Charge. *Scr. Metall. Mater.* **1993**, *20*, 1–8.

9. Murr, L.E.; Niou, C.S.; Sanchez, J.C.; Shih, H.K.; Duplessis, L.; Pappu, S.; Zernow, L. Comparison of Beginning and Ending Microstructures in Metal Shaped Charges as a Means to Explore Mechanisms for Plastic Deformation at High Rates. *J. Mater. Sci.* **1995**, *30*, 2747–2758. [CrossRef]

10. Andrade, U.; Meyers, M.A.; Vecchio, K.S.; Chokshi, A.H. Dynamic Recrystallization in High-Strain, High-Strain-Rate Plastic Deformation of Copper. *Acta Metall. Mater.* **1994**, *42*, 3183–3195. [CrossRef]

11. Gurevitch, A.C.; Murr, L.E.; Shih, H.K.; Niou, C.S.; Advani, A.H.; Manuel, D.; Zernow, L. Characterization and Comparison of Microstructures in the Shaped-Charge Regime: Copper and Tantalum. *Mater. Charact.* **1993**, *30*, 201–216. [CrossRef]

12. Liang, J.W.; Shen, Y.F.; Misra, R.D.K.; Liaw, P.K. High Strength-Superplasticity Combination of Ultrafine-Grained Ferritic Steel: The Significant Role of Nanoscale Carbides. *J. Mater. Sci. Technol.* **2021**, *83*, 131–144. [CrossRef]

13. Held, M.; Kozhushko, A.A. Radial Crater Growing Process in Different Materials with Shaped Charge Jets. *Propellants Explos. Pyrotech.* **1999**, *24*, 339–342. [CrossRef]

14. Zheng, Z.M. Stability of Jet Producecd by Shaped Charge. *Explos. Shock Waves* **1981**, *1*, 6–17.

15. Walters, W.P.; Kecskes, L.J.; Pritchett, J.E. Investigation of a Bulk Metallic Glass as a Shaped Charge Liner Material. In Proceedings of the 23rd International Symposium on Ballistics, Tarragona, Spain, 16–20 April 2006; pp. 31–38.

16. Zhao, Z.; Liu, J.; Guo, W.; Li, S.; Wang, G. Effect of Zn and Ni Added in W-Cu Alloy on Penetration Performance and Penetration Mechanism of Shaped Charge Liner. *Int. J. Refract. Met. Hard Mater.* **2016**, *54*, 90–97. [CrossRef]

17. Bachaga, T.; Zhang, J.; Khitouni, M.; Sunol, J.J. NiMn-Based Heusler Magnetic Shape Memory Alloys: A Review. *Int. J. Adv. Manuf. Technol.* **2019**, *103*, 2761–2772. [CrossRef]

18. Bachaga, T.; Daly, R.; Sunol, J.J.; Saurina, J.; Escoda, L.; Legarreta, L.G.; Hernando, B.; Khitouni, M. Effects of Co Additions on the Martensitic Transformation and Magnetic Properties of Ni–Mn–Sn Shape Memory Alloys. *J. Supercond. Nov. Magn.* **2015**, *28*, 3087–3092. [CrossRef]

19. Bachaga, T.; Daly, R.; Escoda, L.; Sunol, J.J.; Khitouni, M. Influence of Chemical Composition on Martensitic Transformation of MnNiIn Shape Memory Alloys. *J. Therm. Anal. Calorim.* **2015**, *122*, 167–173. [CrossRef]

20. Liu, X.F.; Tian, Z.L.; Zhang, X.F.; Chen, H.H.; Liu, T.W.; Chen, Y.; Wang, Y.J.; Dai, L.H. "Self-Sharpening" Tungsten High-Entropy Alloy. *Acta Mater.* **2020**, *186*, 257–266. [CrossRef]

21. Wang, S.P.; Xu, J. (TiZrNbTa)-Mo High-Entropy Alloys: Dependence of Microstructure and Mechanical Properties on Mo Concentration and Modeling of Solid Solution Strengthening. *Intermetallics* **2018**, *95*, 59–72. [CrossRef]

22. Wu, Y.D.; Cai, Y.H.; Wang, T.; Si, J.J.; Zhu, J.; Wang, Y.D.; Hui, X.D. A Refractory Hf25Nb25Ti25Zr25 High-Entropy Alloy with Excellent Structural Stability and Tensile Properties. *Mater. Lett.* **2014**, *130*, 277–280. [CrossRef]

23. Hou, X.W.; Xiong, W.; Chen, H.H.; Zhang, X.F.; Wang, H.Y.; Dai, L.H. Impact Energy Release and Damage Characteristics of Two High-Entropy Alloys. *Lixue Xuebao Chin. J. Theor. Appl. Mech.* **2021**, *53*, 2528–2540. [CrossRef]

24. Li, W.D.; Xie, D.; Li, D.Y.; Zhang, Y.; Gao, Y.F.; Liaw, P.K. Mechanical Behavior of High-Entropy Alloys. *Prog. Mater. Sci.* **2021**, *118*, 100777. [CrossRef]

25. Lei, Z.F.; Liu, X.J.; Wu, Y.; Wang, H.; Jiang, S.H.; Wang, S.D.; Hui, X.D.; Wu, Y.D.; Gault, B.; Kontis, P.; et al. Enhanced Strength and Ductility in a High-Entropy Alloy via Ordered Oxygen Complexes. *Nature* **2018**, *563*, 546–550. [CrossRef] [PubMed]

26. Bu, Y.Q.; Wang, H.T. Short-Range Order in Multicomponent Alloys. *Adv. Mech.* **2021**, *51*, 915–919.

27. Falk, M.L.; Langer, J.S.; Chen, Y.; Wang, Y.J. Deformation and Failure of Amorphous, Solidlike Materials. *Adv. Mech.* **2021**, *51*, 406–426. [CrossRef]

28. Song, Q.T.; Xu, J. (TiZrNbTa)90Mo10 High-Entropy Alloy: Electrochemical Behavior and Passive Film Characterization under Exposure to Ringer's Solution. *Corros. Sci.* **2020**, *167*, 108513. [CrossRef]

29. Liu, F.; Liaw, P.K.; Zhang, Y. Recent Progress with BCC-Structured High-Entropy Alloys. *Metals* **2022**, *12*, 501. [CrossRef]

30. Chen, J.X.; Chen, Y.; Liu, J.P.; Liu, T.W.; Dai, L.H. Anomalous Size Effect in Micron-Scale CoCrNi Medium-Entropy Alloy Wire. *Scr. Mater.* **2021**, *199*, 113897. [CrossRef]

31. Meng, J.; Liu, T.W.; Wang, H.Y.; Dai, L.H. Ultra-High Energy Absorption High-Entropy Alloy Syntactic Foam. *Compos. Part B Eng.* **2021**, *207*, 108563. [CrossRef]

32. Dong, X.; Zhou, Y.N.; Qu, Y.T.; Wu, M.M.; Sun, Q.; Shi, H.J.; Peng, H.B.; Zhang, Y.X.; Xu, S.; Li, N.; et al. Recrystallization Behavior and Grain Boundary Character Evolution in Co-Cr Alloy from Selective Laser Melting to Heat Treatment. *Mater. Charact.* **2022**, *185*, 111716. [CrossRef]

33. Wu, Y.D.; Li, Y.L.; Liu, X.L.; Wang, Q.J.; Chen, X.M.; Hui, X.D. High Strength NiMnFeCrAlCu Multi-Principal-Element Alloys with Marine Application Perspective. *Scr. Mater.* **2021**, *202*, 113992. [CrossRef]

34. Qiao, Y.; Chen, Y.; Cao, F.H.; Wang, H.Y.; Dai, L.H. Dynamic Behavior of CrMnFeCoNi High-Entropy Alloy in Impact Tension. *Int. J. Impact Eng.* **2021**, *158*, 104008. [CrossRef]

35. Jiang, Z.J.; He, J.Y.; Wang, H.Y.; Zhang, H.S.; Lu, Z.P.; Dai, L.H. Shock Compression Response of High Entropy Alloys. *Mater. Res. Lett.* **2016**, *4*, 226–232. [CrossRef]

36. Zhang, Y.; Zuo, T.T.; Tang, Z.; Gao, M.C.; Dahmen, K.A.; Liaw, P.K.; Lu, Z.P. Microstructures and Properties of High-Entropy Alloys. *Prog. Mater. Sci.* **2014**, *61*, 1–93. [CrossRef]

37. Chen, H.H.; Zhang, X.F.; Dai, L.H.; Liu, C.; Xiong, W.; Tan, M.T. Experimental Study on WFeNiMo High-Entropy Alloy Projectile Penetrating Semi-Infinite Steel Target. *Def. Technol.* **2021**. [CrossRef]

38. Laplanche, G.; Kostka, A.; Reinhart, C.; Hunfeld, J.; Eggeler, G.; George, E.P. Reasons for the Superior Mechanical Properties of Medium-Entropy CrCoNi Compared to High-Entropy CrMnFeCoNi. *Acta Mater.* **2017**, *128*, 292–303. [CrossRef]

39. He, Z.F.; Jia, N.; Wang, H.W.; Liu, Y.; Li, D.Y.; Shen, Y.F. The Effect of Strain Rate on Mechanical Properties and Microstructure of a Metastable FeMnCoCr High Entropy Alloy. *Mater. Sci. Eng. A* **2020**, *776*, 138982. [CrossRef]

40. Cao, F.H.; Wang, Y.J.; Dai, L.H. Novel Atomic-Scale Mechanism of Incipient Plasticity in a Chemically Complex CrCoNi Medium-Entropy Alloy Associated with Inhomogeneity in Local Chemical Environment. *Acta Mater.* **2020**, *194*, 283–294. [CrossRef]

41. Guo, W.Q.; Liu, J.X.; Xiao, Y.; Li, S.K.; Zhao, Z.Y.; Cao, J. Comparison of Penetration Performance and Penetration Mechanism of W-Cu Shaped Charge Liner against Three Kinds of Target: Pure Copper, Carbon Steel and Ti-6Al-4V Alloy. *Int. J. Refract. Met. Hard Mater.* **2016**, *60*, 147–153. [CrossRef]

42. Guo, W.; Li, S.K.; Wang, F.C.; Wang, M. Dynamic Recrystallization of Tungsten in a Shaped Charge Liner. *Scr. Mater.* **2009**, *60*, 329–332. [CrossRef]

43. Murr, L.E.; Shih, H.K.; Niou, C.S. Dynamic Recrystallization in Detonating Tantalum Shaped Charges: A Mechanism for Extreme Plastic Deformation. *Mater. Charact.* **1994**, *33*, 65–74. [CrossRef]

44. Murr, L.E.; Shih, B.K.; Niou, C.S.; Zernow, L. Dynamic Recrystallization in the Shaped Charge Regime. *Scr. Metall. Mater.* **1993**, *29*, 567–572.

45. Esquivel, E.V.; Murr, L.E. Grain Boundary Contributions to Deformation and Solid-State Flow in Severe Plastic Deformation. *Mater. Sci. Eng. A* **2005**, *409*, 13–23. [CrossRef]

46. Wu, Z.; Bei, H.; Otto, F.; Pharr, G.M.; George, E.P. Recovery, Recrystallization, Grain Growth and Phase Stability of a Family of FCC-Structured Multi-Component Equiatomic Solid Solution Alloys. *Intermetallics* **2014**, *46*, 131–140. [CrossRef]

47. Li, Y.J.; Kostka, A.; Savan, A.; Ludwig, A. Phase Decomposition in a Nanocrystalline CrCoNi Alloy. *Scr. Mater.* **2020**, *188*, 259–263. [CrossRef]

48. Schuh, B.; Martin, F.M.; Völker, B.; George, E.P.; Clemens, H.; Pippan, R.; Hohenwarter, A. Mechanical Properties, Microstructure and Thermal Stability of a Nanocrystalline CoCrFeMnNi High-Entropy Alloy after Severe Plastic Deformation. *Acta Mater.* **2015**, *96*, 258–268. [CrossRef]

49. Rajeshwari, K.S.; Sankaran, S.; Kumar, K.C.H.; Rösner, H.; Peterlechner, M.; Esin, V.A.; Divinski, S.; Wilde, G. Grain Boundary Diffusion and Grain Boundary Structures of a Ni-Cr-Fe-Alloy: Evidences for Grain Boundary Phase Transitions. *Acta Mater.* **2020**, *195*, 501–518. [CrossRef]

50. Zhang, S.C.; Jiang, Z.H.; Li, H.B.; Zhang, B.B.; Fan, S.P.; Li, Z.X.; Feng, H.; Zhu, H.C. Precipitation Behavior and Phase Transformation Mechanism of Super Austenitic Stainless Steel S32654 during Isothermal Aging. *Mater. Charact.* **2018**, *137*, 244–255. [CrossRef]

51. Tsai, K.Y.; Tsai, M.H.; Yeh, J.W. Sluggish Diffusion in Co-Cr-Fe-Mn-Ni High-Entropy Alloys. *Acta Mater.* **2013**, *61*, 4887–4897. [CrossRef]

52. Briant, C.L.; Banerji, S.K.; Ritter, A.M. Role of Nitrogen in the Embrittlement of Steel. *Met. Trans A* **1982**, *13*, 1939–1950. [CrossRef]

53. Ming, K.S.; Li, L.L.; Li, Z.M.; Bi, X.F.; Wang, J. Grain Boundary Decohesion by Nanoclustering Ni and Cr Separately in CrMnFeCoNi High-Entropy Alloys. *Sci. Adv.* **2019**, *5*, eaay0639. [CrossRef] [PubMed]